

Article

# Periodic Mesoporous Organosilica Nanoparticles for CO<sub>2</sub> Adsorption at Standard Temperature and Pressure

Paul Kirren <sup>1,\*</sup>, Lucile Barka <sup>1</sup>, Saher Rahmani <sup>1</sup>, Nicolas Bondon <sup>2</sup>, Nicolas Donzel <sup>2</sup>, Philippe Trens <sup>2</sup> , Aurélie Bessière <sup>2</sup> , Laurence Raehm <sup>2</sup>, Clarence Charnay <sup>2</sup>  and Jean-Olivier Durand <sup>2,\*</sup> 

<sup>1</sup> Capgemini Engineering, 75017 Paris, France; lucile.barka@altran.com (L.B.); saher.rahmani@altran.com (S.R.)

<sup>2</sup> ICGM, Univ Montpellier, CNRS, ENSCM, 34293 Montpellier, France; nicolas.bondon@umontpellier.fr (N.B.); nicolas.donzel@umontpellier.fr (N.D.); Philippe.Trens@enscm.fr (P.T.); aurelie.bessiere@umontpellier.fr (A.B.); laurence.raehm@umontpellier.fr (L.R.); clarence.charnay@umontpellier.fr (C.C.)

\* Correspondence: paul.kirren@altran.com (P.K.); jean-olivier.durand@umontpellier.fr (J.-O.D.); Tel.: +33-04-4-48-79-21-27 (J.-O.D.)

**Abstract:** (1) Background: Due to human activities, greenhouse gas (GHG) concentrations in the atmosphere are constantly rising, causing the greenhouse effect. Among GHGs, carbon dioxide (CO<sub>2</sub>) is responsible for about two-thirds of the total energy imbalance which is the origin of the increase in the Earth's temperature. (2) Methods: In this field, we describe the development of periodic mesoporous organosilica nanoparticles (PMO NPs) used to capture and store CO<sub>2</sub> present in the atmosphere. Several types of PMO NP (bis(triethoxysilyl)ethane (BTEE) as matrix, co-condensed with trialkoxysilylated aminopyridine (py) and trialkoxysilylated bipyridine (Etbipy and iPBipy)) were synthesized by means of the sol-gel procedure, then characterized with different techniques (DLS, TEM, FTIR, BET). A systematic evaluation of CO<sub>2</sub> adsorption was carried out at 298 K and 273 K, at low pressure. (3) Results: The best values of CO<sub>2</sub> adsorption were obtained with 6% bipyridine: 1.045 mmol·g<sup>-1</sup> at 298 K and 2.26 mmol·g<sup>-1</sup> at 273 K. (4) Conclusions: The synthesized BTEE/aminopyridine or bipyridine PMO NPs showed significant results and could be promising for carbon capture and storage (CCS) application.

**Keywords:** periodic mesoporous organosilica; sol-gel process; CO<sub>2</sub> adsorption; carbon capture and storage (CCS) application



**Citation:** Kirren, P.; Barka, L.; Rahmani, S.; Bondon, N.; Donzel, N.; Trens, P.; Bessière, A.; Raehm, L.; Charnay, C.; Durand, J.-O. Periodic Mesoporous Organosilica Nanoparticles for CO<sub>2</sub> Adsorption at Standard Temperature and Pressure. *Molecules* **2022**, *27*, 4245. <https://doi.org/10.3390/molecules27134245>

Academic Editor: Igor Djerdj

Received: 30 May 2022

Accepted: 28 June 2022

Published: 30 June 2022

**Publisher's Note:** MDPI stays neutral with regard to jurisdictional claims in published maps and institutional affiliations.



**Copyright:** © 2022 by the authors. Licensee MDPI, Basel, Switzerland. This article is an open access article distributed under the terms and conditions of the Creative Commons Attribution (CC BY) license (<https://creativecommons.org/licenses/by/4.0/>).

## 1. Introduction

In recent years, a significant increase in the concentration of CO<sub>2</sub> into the atmosphere, one of the main greenhouse gases, has given rise to serious concerns, and there is a clear need for greater efforts to reduce CO<sub>2</sub> emissions. Indeed, CO<sub>2</sub> emissions between 1974 and 2004 were greater than those during the 600,000 previous years [1]. Moreover, the current atmospheric concentration of CO<sub>2</sub> reached a value of 414 ppm in 2020, the highest value on Earth for 3 million years [2]. At the same time, CO<sub>2</sub> is an ecological and almost unlimited source of carbon and can be used for many applications such as the production of value-added chemicals and energy products including carbon monoxide [3], methane [4], methanol [5,6], formate [5], methoxide [7], cyclic carbonate or polycarbonate [8], formic acid [9], and urea [10]. Thus, the reduction of CO<sub>2</sub> in the atmosphere has become a very important research topic.

Initially, liquid amine solutions or aqueous alkanolamines such as ethanolamine (MEA), di-ethanolamine (DEA), di-glycolamine (DGA) and *N*-methyldiethanolamine (MDEA) were widely used in the chemical industry to trap acid gases such as carbon dioxide (CO<sub>2</sub>) from gas mixtures [11]. These solutions are able to react and reversibly form other chemical species such as carbamate, carbonate, bicarbonate, etc. [11]. However, this approach to chemical absorption has many disadvantages, such as huge energy consumption for the absorption and regeneration of amines, the high cost of CO<sub>2</sub> evaporation, and

other problems related to amines including poor stability and oxidative degradation of amines, and interference from impure gases such as SO<sub>2</sub>, NO<sub>2</sub>, and NO [12]. Thus, the use of solid adsorbents has gradually replaced this technique.

Several types of material are currently being studied for their CO<sub>2</sub> adsorption properties, such as mesoporous silicas, zeolites, activated carbons, amine-based materials, metal oxides, and MOFs (metal–organic frameworks) [13–16]. The latter have great CO<sub>2</sub> adsorption capacity but many problems remain, such as long and complex syntheses, poor stability depending on temperature and humidity, and complex separation, as well as prices as high as \$10,000 to \$15,000 per kilogram [16–21].

To overcome the problems of conventional liquid amines, new studies have gradually focused on the synthesis of solid adsorbents modified by amines. Recently, porous silica and periodic mesoporous organosilicas (PMOs) have become popular solid adsorbents for CO<sub>2</sub> capture [22,23]. An increase in CO<sub>2</sub> adsorption capacity was observed for PMOs modified with compounds containing amines [24], amines having good affinity with CO<sub>2</sub>, allowing templating diamino-alkyltrimethoxysilanes and leading to lamellar materials after the sol-gel procedure [25]. The impregnation of porous silica adsorbents with amine groups has several advantages such as simple manufacture, low cost, and the ability to load a large number of amines [26]. However, the disadvantage of this technique concerns the amines, which are located at the surface of the porous solids and not inside the pores, which may affect the optimal conditions for CO<sub>2</sub> adsorption. Other scientists have observed a significant improvement in the CO<sub>2</sub> adsorption by using mesoporous silica modified with various grafted amines such as 3-(aminopropyl)triethoxysilane and *N*-[3-(trimethoxysilyl)propyl]ethylenediamine [27,28]. Furthermore, the use of amine-functionalized organosilica for CO<sub>2</sub> capture and valorization is growing significantly [29]. The use of silica-based nanoparticles for the storage of CO<sub>2</sub> has been less described than the use of bulk materials.

In the course of our work concerning the synthesis and applications of periodic mesoporous organosilica nanoparticles (PMO NPs) [30], we were interested in the preparation, of PMO NPs modified with aminopyridine or bipyridine moieties for CO<sub>2</sub> capture. We believed nanoparticles could be very efficient due to their very high developed specific surface area. Indeed, a recent publication reported the high potential of bis(triethoxysilyl)ethane-based nanocubes for CO<sub>2</sub> sequestration [23]. The preparation of bipyridine-based PMOs has been studied by Inagaki, Terasaki, Fontecave and co-workers [31–37] particularly for CO<sub>2</sub> photoreduction. However, to our knowledge, pyridine and bipyridine-based PMO nanoparticles have not yet been investigated for CO<sub>2</sub> capture. Therefore, PMO NPs were prepared through the sol-gel procedure with either 1-(6-aminopyridin-2-yl)-3-(3-(triethoxysilyl)propyl)urea (py), 5,5'-bis(triisopropoxysilyl)-2,2'-bipyridine (iPrbipy) or 5,5'-bis(triethoxysilyl)-2,2'-bipyridine (Etbipy) and 1,2 bis-triethoxysilyl ethane (BTEE) as the PMO NPs matrix. The synthesized PMO NPs were observed by TEM, chemical functionalization was confirmed by FTIR molecular spectroscopy, and the measurement of CO<sub>2</sub> adsorption on the PMO NPs was performed in pure CO<sub>2</sub> gas at 273 K and 298 K.

## 2. Results and Discussion

### 2.1. Effect of the Aminopyridine Moiety on the CO<sub>2</sub> Adsorption

Three BTEE/aminopyridine PMO NPs were synthesized with 1,2-bis(triethoxysilyl)ethane (BTEE) (Figure 1) and 1-(6-aminopyridin-2-yl)-3-(3-(triethoxysilyl)propyl)urea (Figure 2, silylated aminopyridine, (py), prepared through condensation of 2,6-diaminopyridine with 3-(triethoxysilyl)propylisocyanate) [38]. The three types of nanoparticles were obtained through the sol-gel procedure with co-condensation of both precursors by increasing aminopyridine molar fraction: 6% (pyPMO 6 NPs) and 15% (pyPMO 15 NPs). Reference PMO NPs were synthesized with 100% BTEE (PMO 1 NPs).

FTIR molecular spectroscopy analysis was carried out (Figure S1). The obtained spectra allowed the identification of the BTEE precursor with characteristic absorption bands at 1020 cm<sup>-1</sup> and 1160 cm<sup>-1</sup>, respectively, corresponding to Si-O-Si and Si-OH

bonds. The absorption bands corresponding to the aromatic cycle of the pyridine precursor were also observed around  $690\text{--}750\text{ cm}^{-1}$  (C=C and C=N bonds),  $1600\text{ cm}^{-1}$  (amide II band), and  $1690\text{ cm}^{-1}$  (amide I band). The presence of these bands proved the success of the co-condensation between the BTEE and the aminopyridine precursors. Moreover, an increase in the nitrogen content was confirmed by elementary analysis (Table S1).

PMO 1 NPs showed monodisperse nanoparticles of about 80 nm diameter by TEM (Figure 3a and Table 1) and mesoporosity was clearly visible. Dynamic Light Scattering (DLS) in EtOH (Figure S2) confirmed monodispersity with a hydrodynamic diameter of 200 nm. Compared to reference NPs, the addition of aminopyridine led to more polydisperse systems. The pyPMO 6 NPs showed mean diameters of 120 nm but with a standard deviation of 115 nm by TEM (Figure 4a, Table 1). The nanoparticle hydrodynamic diameters distribution was between 100 and 200 nm but aggregates were observed by DLS (Figure S3) at 900 nm. The pyPMO 15 NPs led to smaller nanoparticles of 100 nm diameter but more polydispersed than PMO 1 NPs, (Figure 5a, Table 1) for which DLS showed polydisperse NPs holding 200–500 nm hydrodynamic diameters with large aggregates in the range of 1–2  $\mu\text{m}$  (Figure S4).

**Table 1.** Size distribution, standard deviation values of PMO 1 NPs, pyPMO NPs, analyzed from TEM, specific surface area and pore sizes of PMO 1 NPs, pyPMO NPs analyzed from  $\text{N}_2$  sorption experiments.

PMO NPs (Composition)	PMO 1 (100% BTEE)	PyPMO 6 (94% BTEE/ 6% Aminopyridine)	pyPMO 15 (85% BTEE/ 15% Aminopyridine)
Particle size distribution (nm)	76	120	99
Standard Deviation (nm)	12	114	45
Specific surface area ( $\text{m}^2\text{ g}^{-1}$ )	626	918	805
Pore size (nm)	2.7	2.7	2.5–2.8

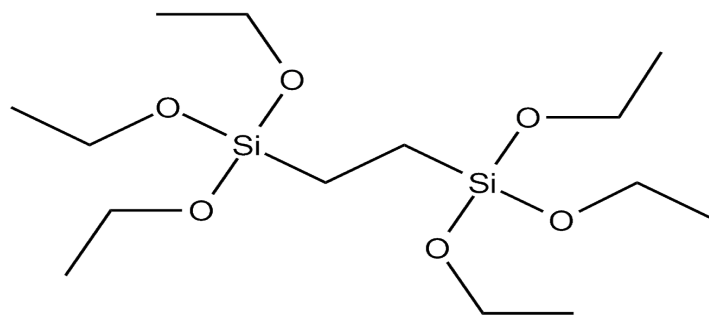


**Figure 1.** Chemical formula of the 1,2-bis(triethoxysilyl)ethane (BTEE) precursor.

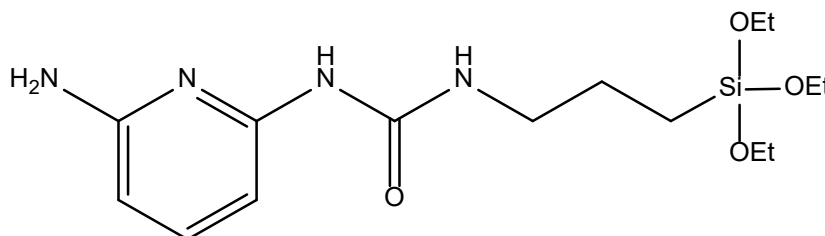


**Figure 2.** Chemical formula of the 1-(6-aminopyridin-2-yl)-3-(3-(triethoxysilyl)propyl)urea (silylated aminopyridine, py).

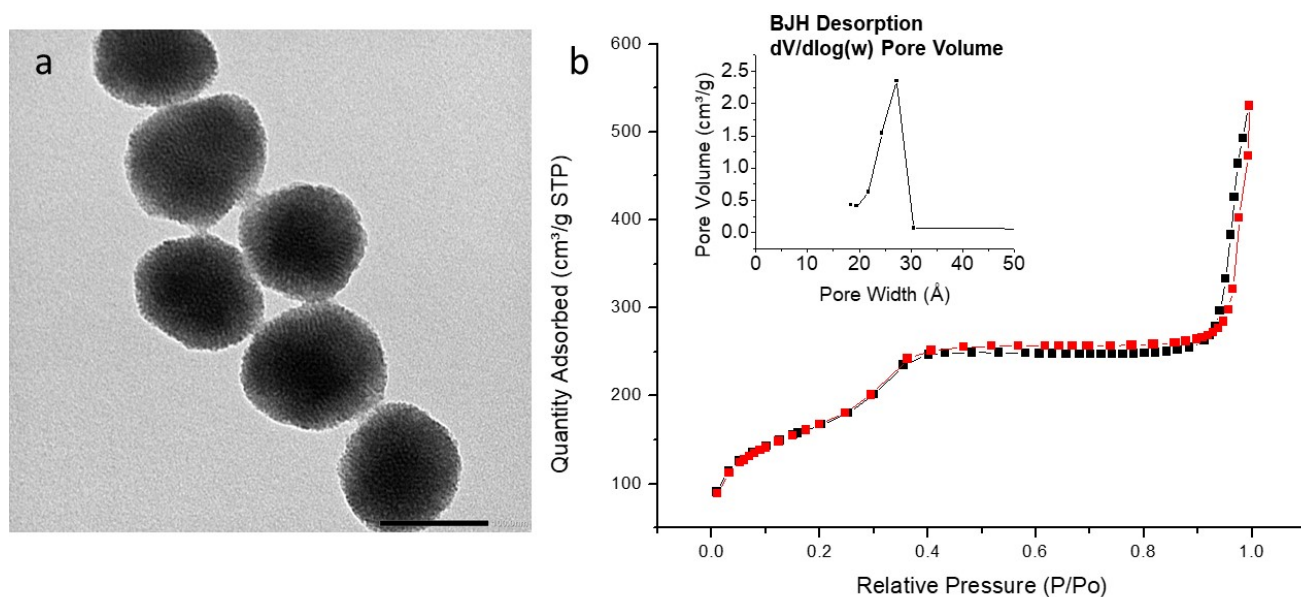


**Figure 3.** (a) TEM image of PMO 1 NPs, scale bar 100 nm. (b) Nitrogen adsorption–desorption at 77 K. Insert BJH desorption ( $dV/d\log(w)$ ) Pore Volume.

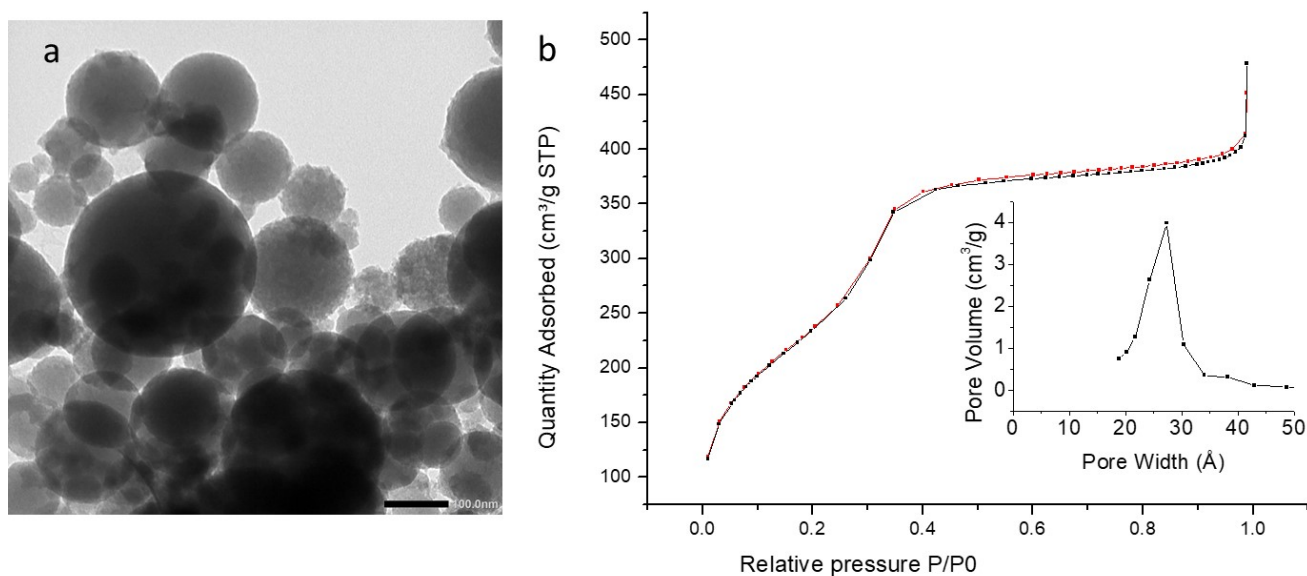


**Figure 4.** (a) TEM image of PyPMO 6 NPs scale bar 100 nm. (b) Nitrogen adsorption–desorption at 77 K. Insert BJH desorption ( $dV/d\log(w)$ ) Pore Volume.

In the case of PMO 1, the shape of the sorption isotherm revealed a type IV isotherm, with a narrow pore size located at 2.7 nm. Its specific surface area was found to be  $626 \text{ m}^2 \cdot \text{g}^{-1}$  (Figure 3b). Higher values of specific surface areas were obtained with pyPMO 6, ( $918 \text{ m}^2 \cdot \text{g}^{-1}$ , Figure 4b) and interestingly, the pore size was similar, compared to PMO 1 (2.7 nm, Figure 4b). The specific surface area seemed to decrease with the increase in the amino pyridine molar fraction to 15% (around  $800 \text{ m}^2 \cdot \text{g}^{-1}$ , Figures 4b and 5b). Note that the contribution of mesopores to the sorption capacity was higher compared to PMO 1, which showed a better structuration of the mesoporosity when using pyridine moieties, even though larger distributed pore sizes from 2.5 to 2.8 nm were observed for the larger aminopyridine fraction materials (Table 1, Figures 4b and 5b).

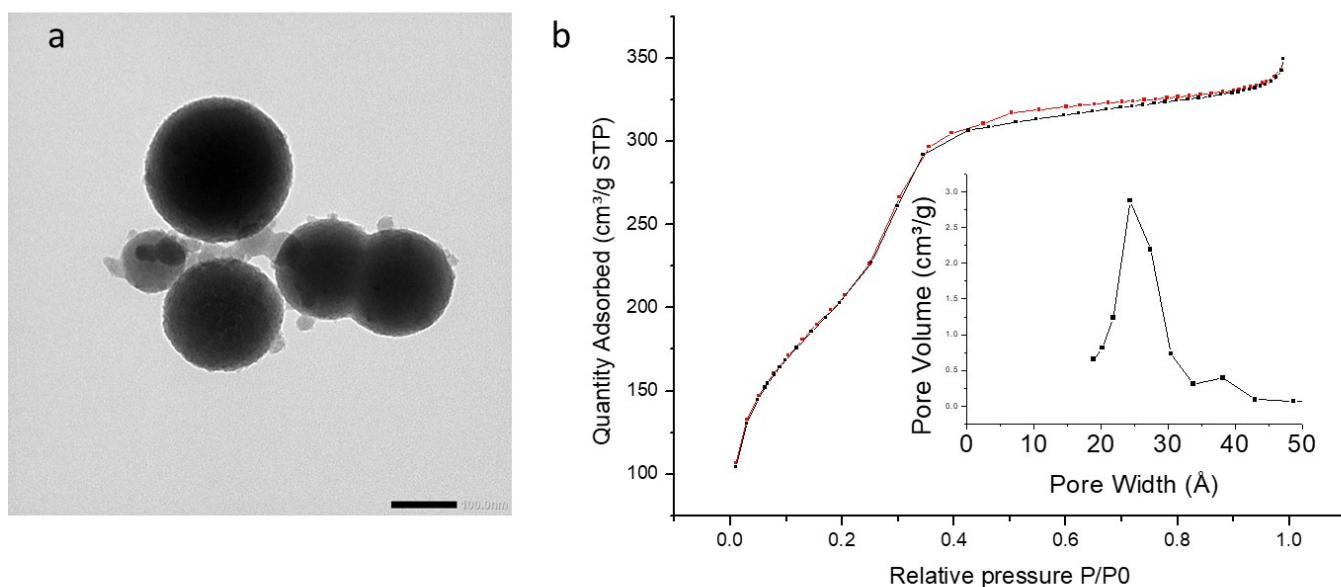


**Figure 5.** (a) TEM image of PyPMO 15 NPs scale bar 100 nm. (b) Nitrogen adsorption–desorption at 77 K. Insert BJH desorption ( $dV/d\log(w)$ ) Pore Volume.

CO<sub>2</sub> adsorption measurements were performed at 298 K and 273 K (Figure 6, Table 2). A slight increase in the CO<sub>2</sub> adsorption capacity with the aminopyridine molar fraction was observed at 298 K. Moreover, an increase of 14% in the CO<sub>2</sub> adsorption was noticed for the pyPMO 15 (0.92 mmol·g<sup>-1</sup>) having the highest aminopyridine content (15%) compared to the 100% BTEE (0.81 mmol·g<sup>-1</sup>). This shows the potential of adding aminopyridine to BTEE for CO<sub>2</sub> capture. However, different results were observed at 273 K, where the CO<sub>2</sub> adsorption for the 100% BTEE was higher than with others PMOs, showing in this case the potential of PMO 1 for CO<sub>2</sub> capture. CO<sub>2</sub> adsorption increases with decreasing temperature. Indeed, adsorption being an exothermic process, increasing the temperature of the system decreases the adsorption capacity [39]. In terms of affinity, it is worth looking at low CO<sub>2</sub> pressure, where the highest interaction sites can be found. The shape of the sorption isotherms is almost linear up to 266 hPa, which confirms the rather poor affinity of these materials for carbon dioxide, regardless of temperature. In these cases, similar Henry's constants can be derived ( $\sim 1.5 \cdot 10^{-3}$  mmol·g<sup>-1</sup>·Pa<sup>-1</sup> at 298 K).

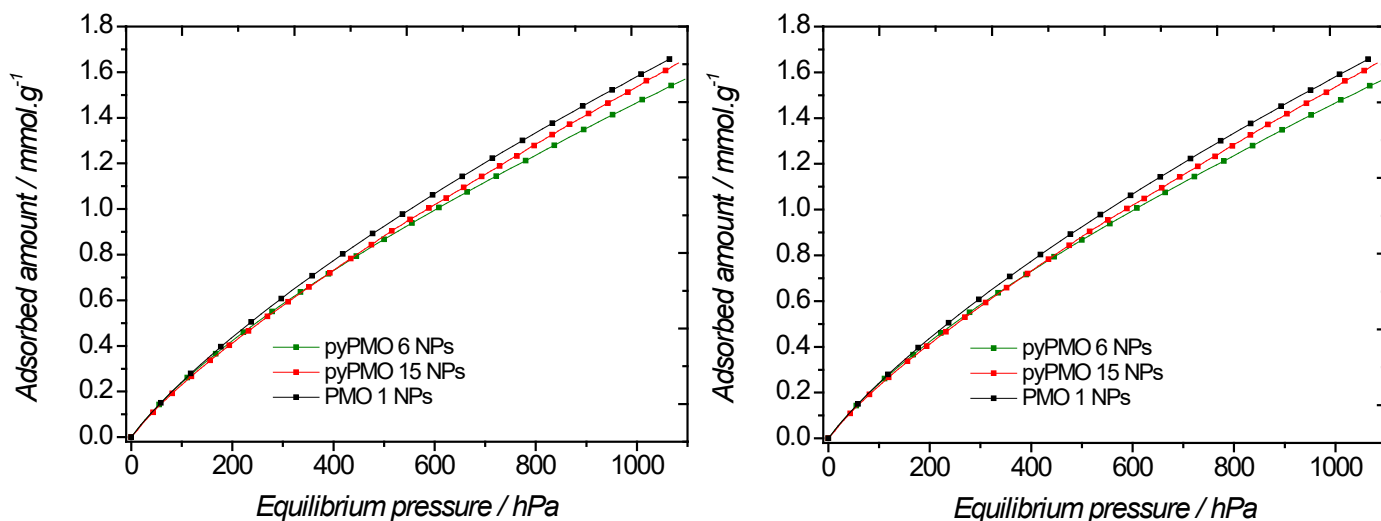


**Figure 6.** Evolution of the CO<sub>2</sub> adsorption of BTEE/pyPMO NPs with different pyridine molar fractions versus absolute pressure, at 298 K (left) and 273 K (right).

**Table 2.** CO<sub>2</sub> adsorption capacity (expressed as mmol·g<sup>-1</sup>) at 10<sup>5</sup> Pa for the BTEE/pyridine PMO NPs.

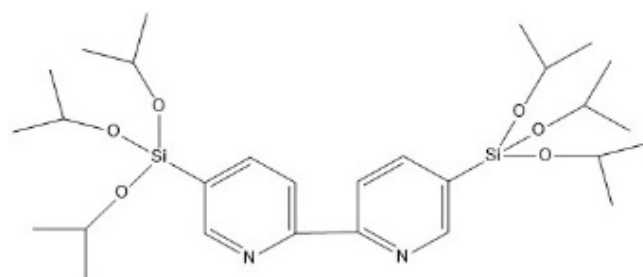
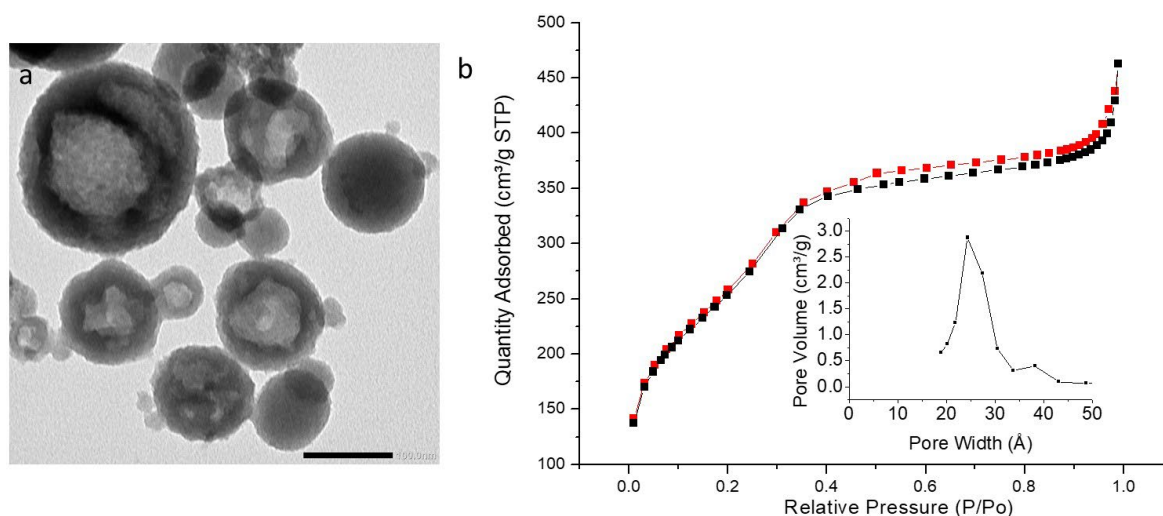
PMO	T = 298 K	T = 273 K
PMO 1	0.81	1.60
pyPMO 6	0.83	1.48
pyPMO 15	0.92	1.55

## 2.2. Effect of the *i*Prbipyridine Moiety on the CO<sub>2</sub> Adsorption

Three BTEE/*i*Prbipyridine PMO NPs were synthesized with BTEE and 5,5'-bis(triisopropoxysilyl)-2,2'-bipyridine (*i*Prbipy) (Figure 7) by increasing the *i*Prbipyridine molar fraction from 6 to 15%: 6% (*i*PrbipyPMO 6), 10% (*i*PrbipyPMO 10) and 15% (*i*PrbipyPMO 15).

FTIR molecular spectroscopy analysis (Figure S5) revealed the success of the co-condensation between the BTEE and the *i*Prbipyridine precursors, as the pyridine precursors exhibited the same characteristic absorption bands. Indeed, a new absorption band, centered at 750 cm<sup>-1</sup> appeared. This band can be attributed to the C=N bonds from the two aromatic cycles. An increase in the intensity of this band with the bipyridine molar fraction was observed, due to the four-fold increase in nitrogen content (Table S2). This offers convincing proof of the success of the polycondensation between the BTEE and the bipyridine precursors.

TEM images (Figures 8a, 9a and 10a) showed highly porous (hollow systems) but polydispersed nanoparticles with a mean diameter of 92 nm (*i*PrbipyPMO 6) or 111 nm (*i*PrbipyPMO 10). DLS in EtOH confirmed polydispersity of *i*PrbipyPMO 6 with two populations centered at 200 nm and 900 nm (nanoparticles and aggregates, respectively, Figure S6). For *i*PrbipyPMO 10 and *i*PrbipyPMO 15 the populations were centered between 500–600 nm, which is characteristic of dispersed aggregates of nanoparticles (Figures S7 and S8).

**Figure 7.** Chemical formula of the 5,5'-bis(triisopropoxysilyl)-2,2'-bipyridine (*i*Prbipy) precursor.**Figure 8.** (a) TEM image of *i*PrbipyPMO 6 scale bar 100 nm. (b) Nitrogen adsorption–desorption at 77 K. Insert BJH desorption (dV/dlog(w)) Pore Volume.

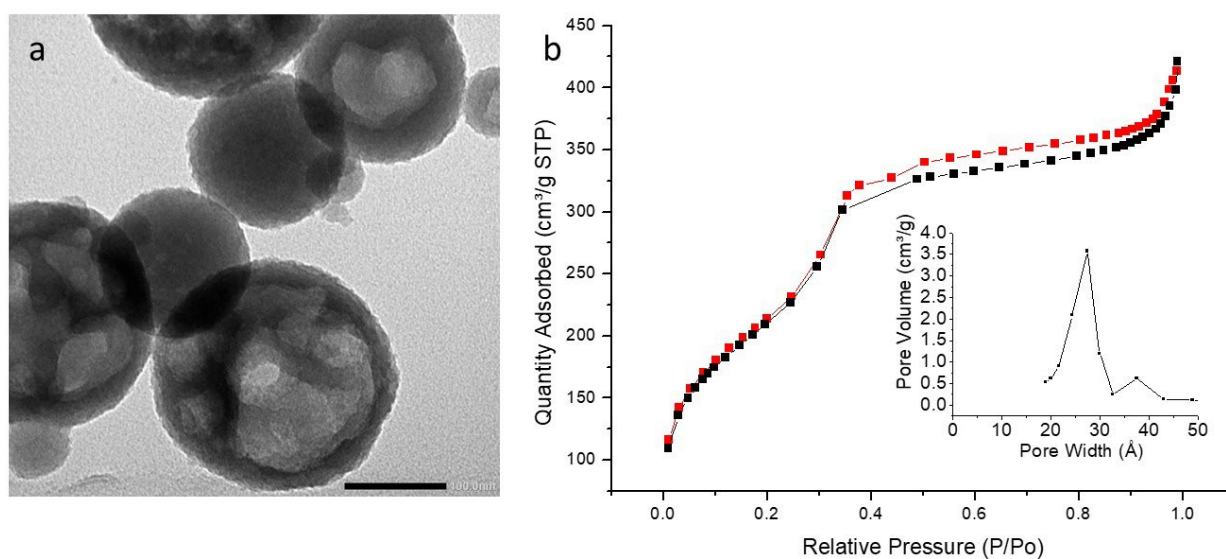


**Figure 9.** (a) TEM image of iPrbiPyPMO 10 scale bar 100 nm. (b) Nitrogen adsorption–desorption at 77 K. Insert BJH desorption ( $dV/d\log(w)$ ) Pore Volume.

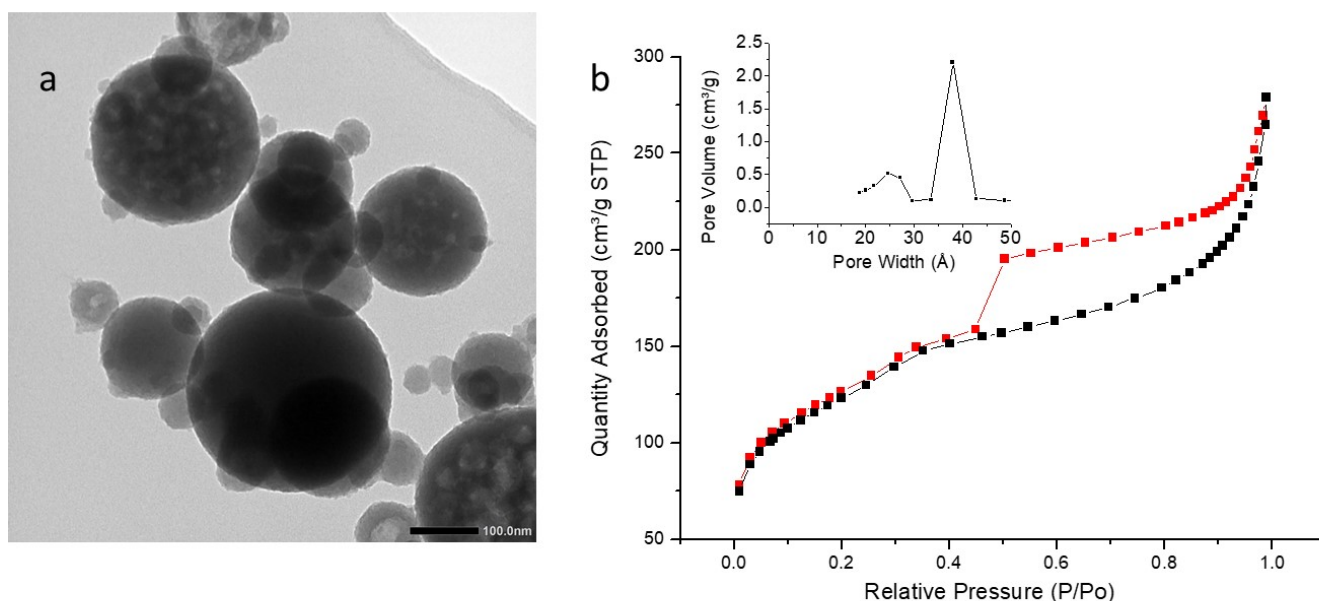


**Figure 10.** (a) TEM image of iPrbiPyPMO 15 scale bar 100 nm. (b) Nitrogen adsorption–desorption at 77 K. Insert BJH desorption ( $dV/d\log(w)$ ) Pore Volume.

The three iPrbiPyPMO materials were mesoporous, as indicated by a clear uptake at intermediate relative pressures followed by saturation (Figures 8b, 9b and 10b, Table 3). However, this saturation became less clear as the bipyridine moieties fraction increased. Concomitantly, the hysteresis loop increased. The shape of the hysteresis loop (H3 type) indicates the presence of hollow materials, in which desorption occurs through small mesopores compared to the size of the cavities. The specific surface area with the addition of 6% and 10% bipyridine was higher compared to that of PMO 1 ( $958 \text{ m}^2 \cdot \text{g}^{-1}$  and  $796 \text{ m}^2 \cdot \text{g}^{-1}$ ). The derivation of the pore size distribution using the desorption branches of the sorption isotherms gave two populations of pores, the most important located at  $\sim 2.5 \text{ nm}$  and a second one located at  $3.7 \text{ nm}$ . The latter is reminiscent of cavitation effects when desorption occurs in small mesopores connected to large cavities, which is precisely the case with hollow materials.

In terms of CO<sub>2</sub> capture, the bipyridine-based PMOs behaved differently compared to the aminopyridine-based PMOs (Figure 11, Table 4). At low pressure, the four traces were different, and they were almost superposed in the case of aminopyridine-based PMOs. In the latter case, the influence of aminopyridine moieties was found to be moderate at low pressure, as the sorption capacity was close to that of PMO 1. Using bipyridine moieties, PMO 1 had the lowest CO<sub>2</sub> sorption capacity, which indicates a clear interaction between bipyridine moieties and carbon dioxide. Quantitatively, the highest CO<sub>2</sub> adsorption capacity was obtained with iPrbipyPMO 6 with 6% iPrbipyridine (1.045 mmol·g<sup>-1</sup> at 298 K and 2.26 mmol·g<sup>-1</sup> at 273 K). A straightforward explanation is that the greatest specific surface area is found with this material, compared to the other PMOs of the series (Figure 8b, Table 3). In terms of sorption efficiency, it is worth differentiating the sorption capacity per square meter. This calculation yields different sorption capacities: 1.09 μmol·m<sup>-2</sup>, 0.992 μmol·m<sup>-2</sup>, and 1.97 μmol·m<sup>-2</sup> for iPrbipyPMO 6, iPrbipyPMO 10, and iPrbipyPMO 15, respectively. This trend shows that bipyridine moieties interact with CO<sub>2</sub>, even though other effects may come into play, such as structuration, pore blocking, and so on. At 273 K, it can be noted that the sorption capacities of the bipyridine-based PMOs reach those of PMO 1, which indicates that even if the CO<sub>2</sub>/bipyridine-based PMOs' affinity is greater compared to PMO 1, their sorption capacities are similar (apart from 6% bipyridine).

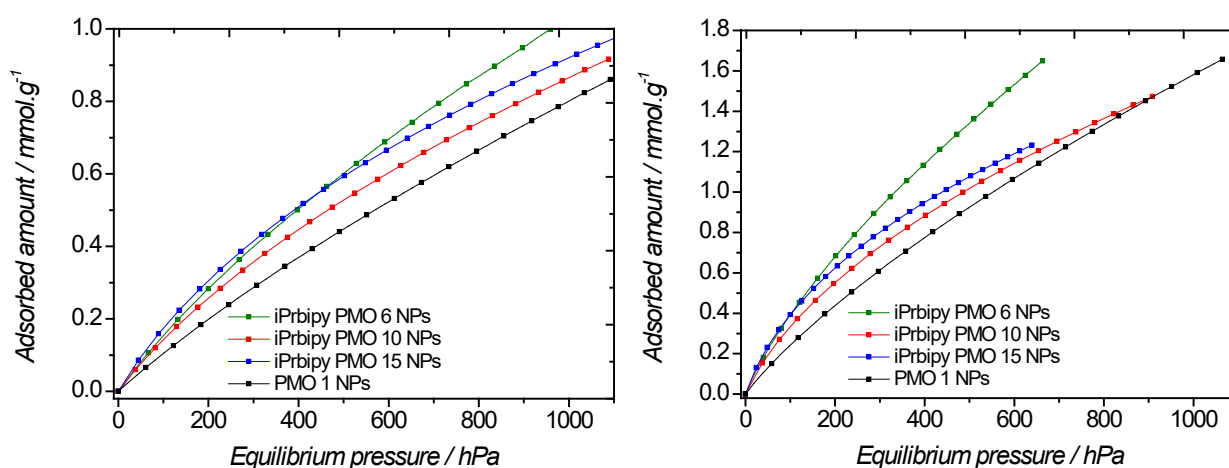


**Figure 11.** Evolution of the CO<sub>2</sub> adsorption of BTEE/iPrbipyridine PMO NPs with different bipyridine molar fractions versus absolute pressure at 298 K (left) and 273 K (right).

**Table 3.** CO<sub>2</sub> adsorption capacity (expressed as mmol·g<sup>-1</sup>) at 10<sup>5</sup> Pa for the BTEE/bipyridine PMO NPs.

PMO	T = 298 K	T = 273 K
iPrbipyPMO 6	1.04	2.26
iPrbipyPMO 10	0.79	1.57
iPrbipyPMO 15	0.85	1.56

**Table 4.** Size distribution, standard deviation values of iPrbipyPMO NPs, analyzed from TEM, specific surface area and pore sizes of iPrbipyPMO NPs analyzed from N<sub>2</sub> sorption experiments.

PMO (Composition)	iPrbipyPMO 6 (94% BTEE/ 6% Bipyridine)	iPrbipyPMO 10 (90% BTEE/ 10% Bipyridine)	iPrbipyPMO 15 (85% BTEE/ 15% Bipyridine)
Particle size distribution (nm)	93	111	102
Standard Deviation (nm)	46	61	72
Specific surface area (m <sup>2</sup> ·g <sup>-1</sup> )	958	796	432
Pore size (nm)	2.5	2.5	2.5

### 2.3. Effect of the Etbipyridine Moiety on the CO<sub>2</sub> Adsorption

Three BTEE/Etbipyridine PMO NPs were synthesized with BTEE and 5,5'-bis(triethoxysilyl)-2,2'-bipyridine (Etbipy) (Figure 12), by increasing the Etbipyridine molar fraction: 6% (EtbipyPMO 6), 10% (EtbipyPMO 10) and 15% (EtbipyPMO 15).

On the IR spectra side, (Figure S9) as for the synthesized PMO NPs with the *i*Prbipyridine precursor, the characteristic absorption band of the C=N aromatic bond located around 750 cm<sup>-1</sup> increased with the Etbipyridine molar fraction, a feature of the co-condensation between the BTEE and the Etbipyridine precursors. This band did not appear for the aminopyridine precursor, probably due to the difference in chemical structure with the presence of two aromatic cycles with nitrogen for the *i*Prbipyridine and the Etbipyridine, against only one aromatic cycle for the aminopyridine precursor. An increase in the percentage of nitrogen with the increase in the molar fraction of Etbipyridine was observed. However, these percentages were lower than with the other precursors (Table S3).

TEM images (Figures 13a, 14a and 15a) showed the formation of larger particles than pyPMO NPs and *i*Pr PMO NPs, with diameters ranging from 300 to 588 nm. A significant standard deviation was also observed for the three PMO NPs (Table 5). Hollow structure was not observed. DLS analysis revealed a single population of nanoparticles with mean hydrodynamic diameter around 1100 nm, due to aggregation of the NPs in EtOH (Figures S10–S12).

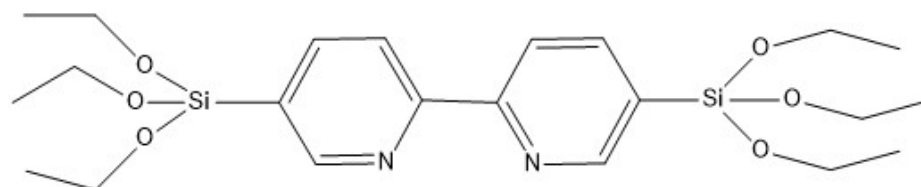


Figure 12. Chemical formula of the 5,5'-bis(triethoxysilyl)-2,2'-bipyridine (Etbipy) precursor.

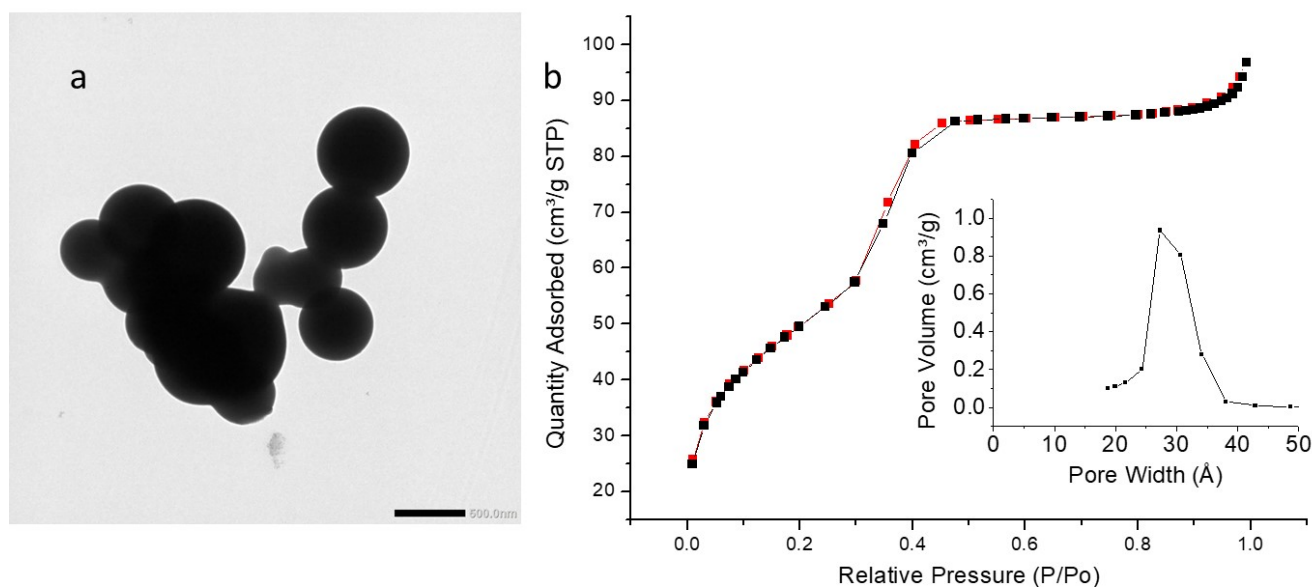
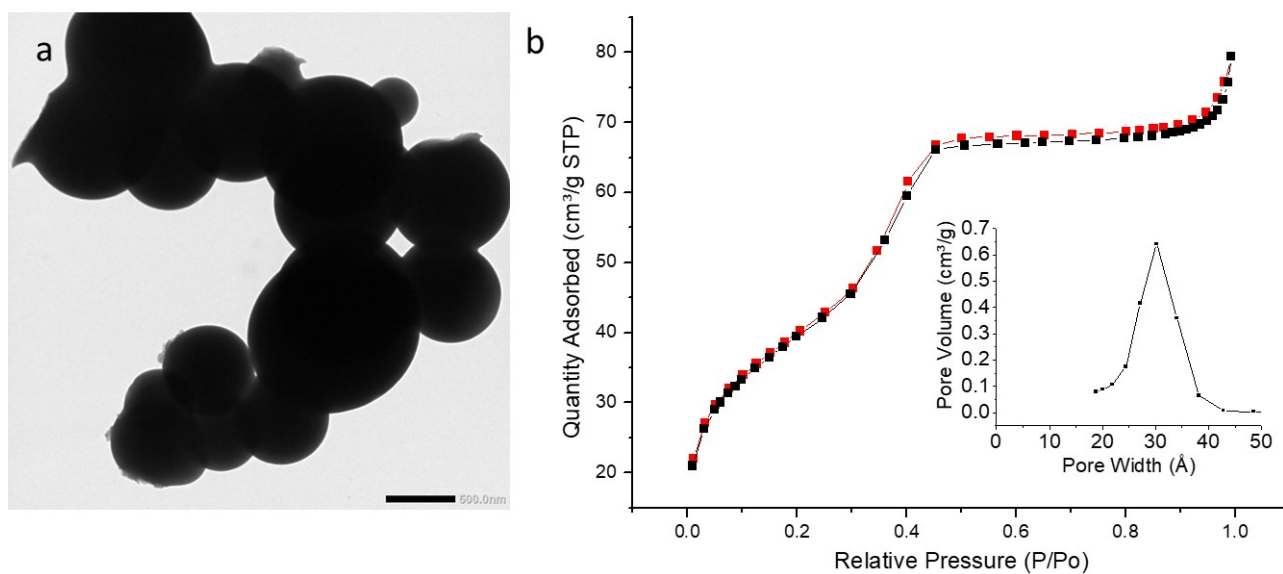
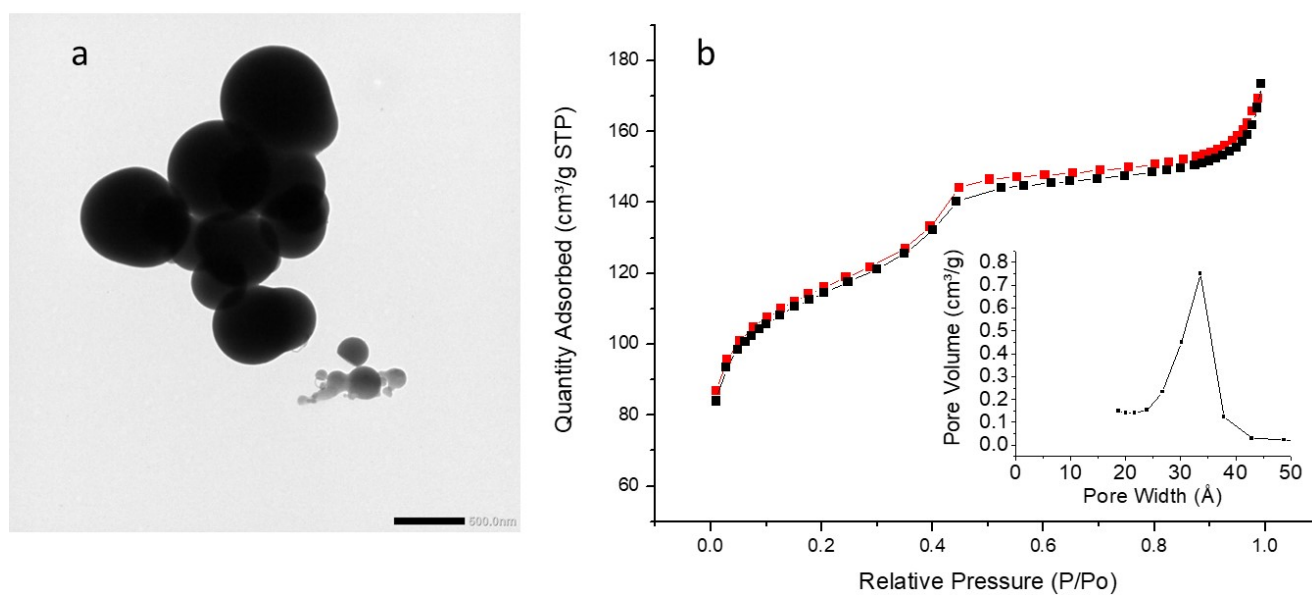


Figure 13. (a) TEM image of EtbiPyPMO 6 scale bar 500 nm. (b) Nitrogen adsorption–desorption at 77 K. Insert BJH desorption (dV/dlog(w)) Pore Volume.



**Figure 14.** (a) TEM image of EtbiPyPMO 10 scale bar 500 nm. (b) Nitrogen adsorption–desorption at 77 K. Insert BJH desorption ( $dV/d\log(w)$ ) Pore Volume.



**Figure 15.** (a) TEM image of EtbiPyPMO 15 scale bar 500 nm. (b) Nitrogen adsorption–desorption at 77 K. Insert BJH desorption ( $dV/d\log(w)$ ) Pore Volume.

**Table 5.** Size distribution and standard deviation values of the BTEE/Etbipyridine PMO NPs analyzed from  $N_2$  sorption experiments.

PMO (Composition)	EtbiPyPMO 6 (94% BTEE/6% Etbipyridine)	EtbiPyPMO 10 (90% BTEE/10% Etbipyridine)	EtbiPyPMO 15 (85% BTEE/15% Etbipyridine)
Particle size distribution (nm)	301	588	437
Standard Deviation (nm)	287	300	144
Specific surface area ( $m^2 \cdot g^{-1}$ )	181	143	372
Pore size (nm)	2.8	3.0	3.4

In terms of textural properties (Figures 13b, 14b and 15b), the sorption isotherms obtained with the EtbiPyPMO series belong to type IV, as found for the other series studied

in this work. In this particular case, the saturation plateaus were very flat, which shows that these materials are purely mesoporous, without side adsorption in voids. This is confirmed by the absence of hysteresis loops for these PMOs, which suggests that they are not aggregated. The mesopore volume decreased from 41% down to 27% for increasing fractions of ethoxybipyridine moieties. At the same time, the surface areas obtained were lower compared to PMO 1 NPs, but also compared to other PMOs studied in this work. This could be due to the greater thickness of the pores' walls as a consequence of the condensation of the ethoxybipyridine moieties. Additionally, the average mesopore size was found to slightly increase for growing fractions of ethoxybipyridine moieties (from 2.8 nm up to 3.4 nm).

The carbon dioxide sorption isotherms obtained with this series of PMOs strongly depended on the fraction of Etbipyridine fraction (Figure 16, Table 6). This trend was even more pronounced compared to the iPrbipyridine series. Indeed, at low pressure, the slopes were completely different, regardless of temperature, and the uptake at  $10^5$  Pa was also different. Intriguingly, iPrbipyridine PMO 10 showed a greater affinity compared to the other PMOs, however this feature was not present at 273 K. Two materials showed a poor  $\text{CO}_2$  capture capacity compared to PMO 1, namely the Etbipyridine 6 and Etbipyridine 10 PMOs. On the other hand, Etbipyridine PMO 15 exhibited better sorption capacities than PMO 1. We further derived the adsorbed amount per square meter to evidence the efficiency of these materials. The adsorbed amounts were found to be  $1.2 \mu\text{mol}\cdot\text{m}^{-2}$ ,  $2 \mu\text{mol}\cdot\text{m}^{-2}$ ,  $4 \mu\text{mol}\cdot\text{m}^{-2}$ , and  $2.5 \mu\text{mol}\cdot\text{m}^{-2}$  for PMO 1 NPs, EtbipyPMO 6 NPs, EtbipyPMO 10 NPs, and EtbipyPMO 15 NPs, respectively, which shows that carbon dioxide interacts with Etbipyridine moieties more than with PMO 1 NPs.

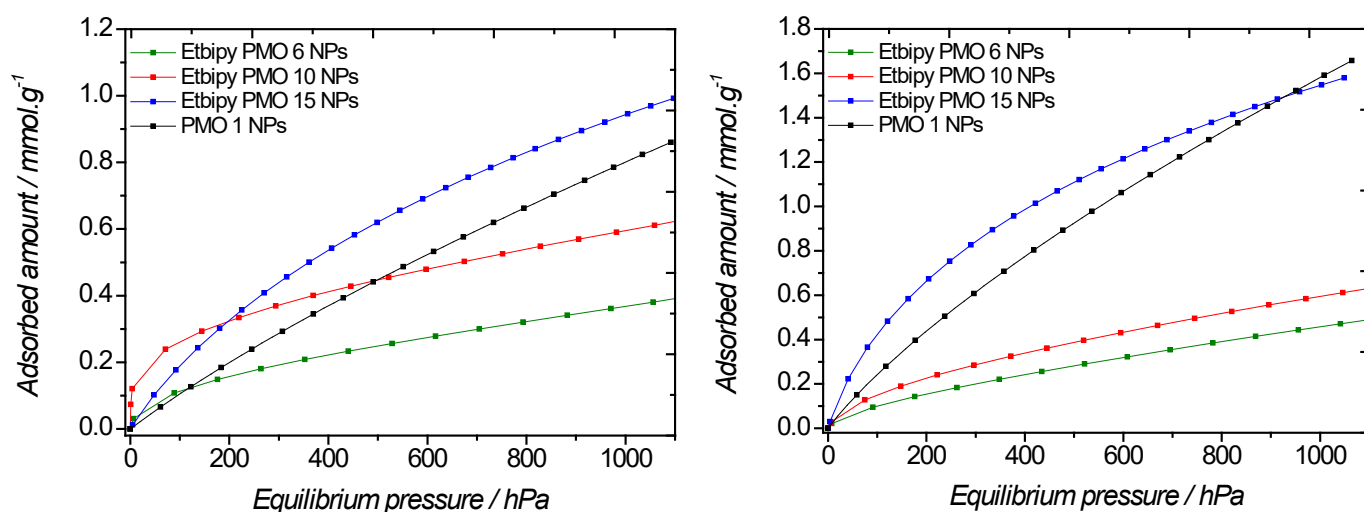


**Figure 16.** Evolution of the  $\text{CO}_2$  adsorption of BTEE/Etbipyridine PMO NPs with different Etbipyridine molar fractions versus absolute pressure at 298 K (left) and 273 K (right).

Despite the similarity of the chemical structures between the iPrbipyridine and the Etbipyridine precursors, the  $\text{CO}_2$  adsorption is favored (as for the aminopyridine) for a large Etbipyridine molar fraction (15%), and for a low iPrbipyridine molar fraction (6%).

**Table 6.**  $\text{CO}_2$  sorption capacity of the BTEE/Etbipyridine PMO NPs.

PMO	Adsorption at $10^5$ Pa at 298 K ( $\text{mmol}\cdot\text{g}^{-1}$ )	Adsorption at $10^5$ Pa at 273 K ( $\text{mmol}\cdot\text{g}^{-1}$ )
EtbipyPMO 6	0.37	0.46
EtbipyPMO 10	0.60	0.60
EtbipyPMO 15	0.95	1.66

#### 2.4. Selection of the Best PMOs for the CO<sub>2</sub> Capture

Our results compare well with some of the studies which use amine-modified porous silicas for CO<sub>2</sub> capture and the field has been comprehensively reviewed [40,41]. Note that these studies concern bulk materials. For instance, in our case, at 1 atm, the adsorbed CO<sub>2</sub> amount obtained for the best materials is around 1 mmol/g which corresponds to 45 mg/g. Using APTES-grafted MCM-41, Mello et al. obtained 33 mg/g at 20 °C [42] with APTES-grafted MCM-48; Kim et al. obtained 35 mg/g [43]. However, using MCM-41 with larger mesopores grafted with diethanolamine, 104 mg/g of CO<sub>2</sub> could be adsorbed at very low pressure (0.05 atm) [44].

Under more favourable conditions (lower temperature [45], higher pressure [42], or highly selective polyethyleneimine [46]), larger CO<sub>2</sub> amounts have been captured (135 mg/g).

Finally, according to the different types of synthesized PMO NPs, the highest CO<sub>2</sub> adsorption values were obtained at 298 K for:

- iPrbipyPMO 6 (94% BTEE/6% iPrbipyridine): 1.04 mmol·g<sup>-1</sup>;
- EtbipyPMO 15 (85% BTEE/15% Etbipyridine): 0.95 mmol·g<sup>-1</sup>;
- pyPMO 15 (85% BTEE/15% aminopyridine): 0.92 mmol·g<sup>-1</sup>.

Compared to the 100% BTEE (0.81 mmol·g<sup>-1</sup>), higher CO<sub>2</sub> adsorption capacity was observed with 29% (iPrbipyPMO 6 NPs), 17% (EtbipyPMO 15 NPs) and 14% (pyPMO 15 NPs), which showed the strong impact of the polycondensation between the BTEE and the precursor containing aminopyridine groups, amines having an important affinity with the CO<sub>2</sub> molecule. On the one hand, the best CO<sub>2</sub> adsorption values were obtained with the bipyridine and the Etbipyridine precursors, proving the importance of the presence of two aromatic cycles with nitrogen for CO<sub>2</sub> capture. On the other hand, CO<sub>2</sub> adsorption was favored with a large aminopyridine (or Etbipyridine) molar fraction (15%), and with a low iPrbipyridine molar fraction (6%). In terms of CO<sub>2</sub>/PMO affinity, these three materials exhibited different features, as can be seen in Figure 17, which presents plots of the isosteric heat of adsorption.

In the case of the pyridine-based material, the enthalpy of adsorption was rather weak, close to the enthalpy of condensation of CO<sub>2</sub> at 298 K, that is 16.7 kJ·mol<sup>-1</sup> at room temperature [47]. Furthermore, the shape of the enthalpic curve was rather flat, which indicates that this material is seen as homogeneous by carbon dioxide species. The other materials were more interesting in terms of affinity, as the enthalpy of adsorption was close to -30 kJ·mol<sup>-1</sup> at low coverage, which indicates a high CO<sub>2</sub>/PMO interaction. However, the high interaction sites did not dominate the sorption processes, as shown by the fact that the enthalpy curves strongly decrease as coverage increases. This is especially true for Etbipyridine-based PMO, whereas in the case of the iPrbipyridine analogue, there is an inflexion in the curve (located at  $\theta = 0.2$ ) which suggests two sorption regimes. At very low coverage, sorption is likely to mostly happen on the iPrbipyridine moieties, while at higher coverage, sorption proceeds on the whole surface of the material. To investigate these observations, we performed two sorption cycles using the procedure described in the experimental section (Figure 18). However, between the two cycles, iPrbipy PMO 6 was subjected to a re-activation stage at 60 °C for 2 h under vacuum. The two sorption isotherms were found to be close to one another, however with ~15% difference at 10<sup>5</sup> Pa. This difference can therefore be accounted for by the interaction sites of iPrbipy PMO 6. In the case of the other materials, for which less interaction was found, it can be anticipated that consecutive sorption isotherms would lead to closer sorption isotherms.

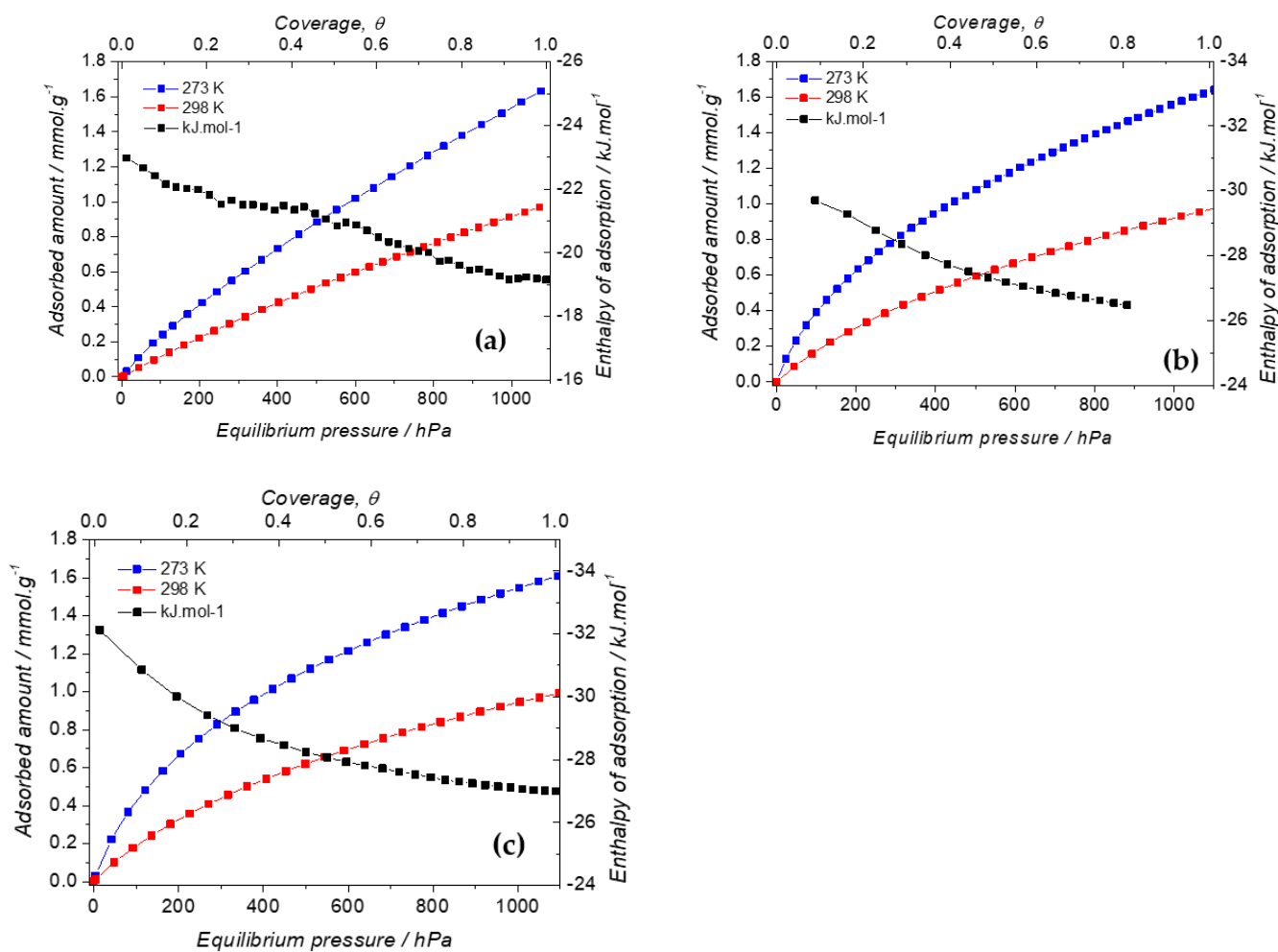


**Figure 17.** Isosteric heat of adsorption for the selected PMOs: (a) pyPMO 15; (b) iPrbipy PMO 6; (c) EtbipyPMO 15. The maximum coverage,  $\theta$ , has been defined as the ratio between the adsorbed amount and the adsorbed amount taken at  $10^5$  Pa.

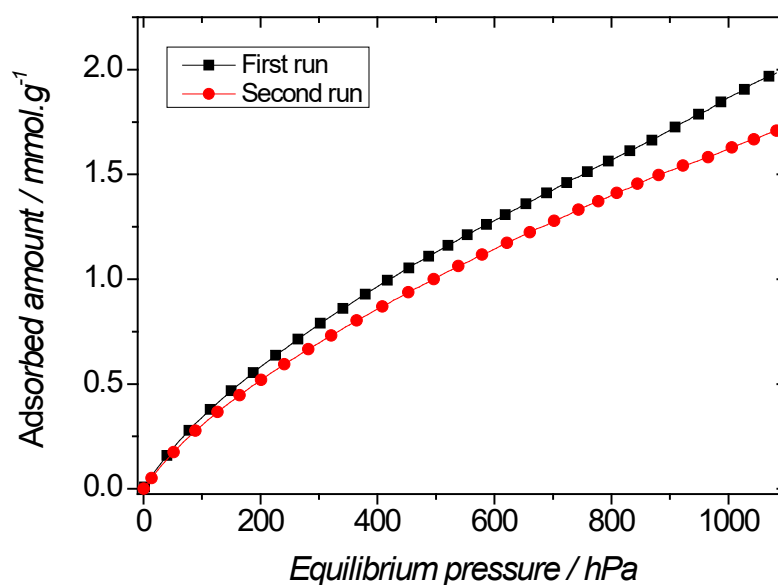


**Figure 18.** CO<sub>2</sub> sorption isotherms by iPrbipy PMO 6 at 273 K. (Squares) first sorption isotherm; (Circles) second sorption isotherm after reactivation at 60 °C for 2 h under secondary vacuum.

It is therefore interesting to discuss the properties of these PMOs not only in terms of their sorption capacity, but also in terms of their sorption efficiency, as these two aspects of the sorption process lead to the choice of the appropriate material. Where traces of CO<sub>2</sub> are concerned, a high affinity is required, whereas if large amounts of CO<sub>2</sub> must be adsorbed, large CO<sub>2</sub> sorption capacities should prevail.

### 3. Materials and Methods

Cetyltrimethylammonium bromide (CTAB), sodium hydroxide, 3-(triethoxysilyl)propylisocyanate, 1,2-bis(triethoxysilyl)ethane (BTEE), 2,6-diaminopyridine, ammonium nitrate (NH<sub>4</sub>NO<sub>3</sub>), and potassium bromide, were purchased from Sigma-Aldrich (St. Louis, MO, USA). 5,5'-bis(triisopropoxysilyl)-2,2'-bipyridine was purchased from TCI. 5,5'-bis(triethoxysilyl)-2,2'-bipyridine was purchased from Sikemia. Absolute ethanol was purchased from Fisher Chemicals.

#### 3.1. Synthesis of BTEENPs

For CO<sub>2</sub> adsorption, PMO NPs were synthesized using the sol-gel procedure. A total of 250 mg of CTAB as the surfactant ( $6.86 \times 10^{-4}$  mol), 437  $\mu$ L of NaOH solution ( $2 \text{ mol}\cdot\text{L}^{-1}$ ), and 333  $\mu$ L of 1,2-bis(triethoxysilyl)ethane (or BTEE, Figure 1) ( $9 \times 10^{-4}$  mol) were dissolved in 60 mL of deionized water. The mixture was stirred for 2 h at 80 °C/750 rpm. The reaction mixture was cooled to room temperature and centrifuged for 20 min at 20,000 rpm. The CTAB surfactant was removed by 45 min sonication at 40 °C, with a 30 mL solution of ammonium nitrate (NH<sub>4</sub>NO<sub>3</sub>) in EtOH ( $6 \text{ g}\cdot\text{L}^{-1}$ ), followed by one water wash and two EtOH washes (30 mL each). BTEENPs were dried in a vacuum oven at 70 °C.

#### 3.2. Synthesis of BTEE-Aminopyridinenps/BTEE-iPrbipyridineNPs/BTEE-EtbipyridineNPs

With regard to the BTEENPs, the BTEE-aminopyridineNPs, the BTEE-iPrbipyridine NPs and the BTEE-Etbipyridine NPs were synthesized by the sol-gel procedure. The chemical formulas of each precursor are presented in Figures 2, 7 and 12. The synthesis was adapted from [48]. For all the PMOs, a total of 1.04 g of CTAB ( $2.85 \times 10^{-3}$  mol) and 0.472 g of NaOH solution ( $1.18 \times 10^{-2}$  mol) were dissolved in 31.8 mL of deionized water. The total number of moles for the two precursors (BTEE/aminopyridine or iPrbipyridine or Etbipyridine) was  $5.18 \times 10^{-3}$ , the molar fraction being different. For example, with iPrPMO 6 (94% ethane/6% bipyridine), a solution of 1.8 mL of BTEE ( $4.86 \times 10^{-3}$  mol) and 0.181 g of 5,5'-bis(triisopropoxysilyl)-2,2'-bipyridine ( $3.20 \times 10^{-4}$  mol) was added and the mixture was stirred for 24 h at room temperature, at 750 rpm. The reaction was stirred for 2 h at 95 °C and 750 rpm. The reaction mixture was cooled to room temperature and centrifuged for 20 min at 20,000 rpm. Surfactant was removed by 45 min sonication at 40 °C, with a 30 mL solution of ammonium nitrate (NH<sub>4</sub>NO<sub>3</sub>) in EtOH ( $6 \text{ g}\cdot\text{L}^{-1}$ ), followed by one diethyl ether wash and two EtOH washes (30 mL each). Finally, the NPs were dried in a vacuum oven at 70 °C. This process was mainly used with the iPrbipyridine and the Etbipyridine precursors (Figures 6 and 10). Next, 2,6-diaminopyridine was silylated with 3-(triethoxysilyl)propylisocyanate to produce the silylated precursor 1-(6-aminopyridin-2-yl)-3-(3-(triethoxysilyl)propyl)urea (py), the chemical structure of which is presented in Figure 2. The protocol established by Cho et al. was applied for the silylation process [38]. Finally, the BTEE/pyPMOs were synthesized by hydrolysis and polycondensation of 1-(6-aminopyridin-2-yl)-3-(3-(triethoxysilyl)propyl)urea and 1,2(-bis(triethoxysilyl)ethane according to the previous conditions. The process synthesis of the PMO NPs is presented in Figure 19.

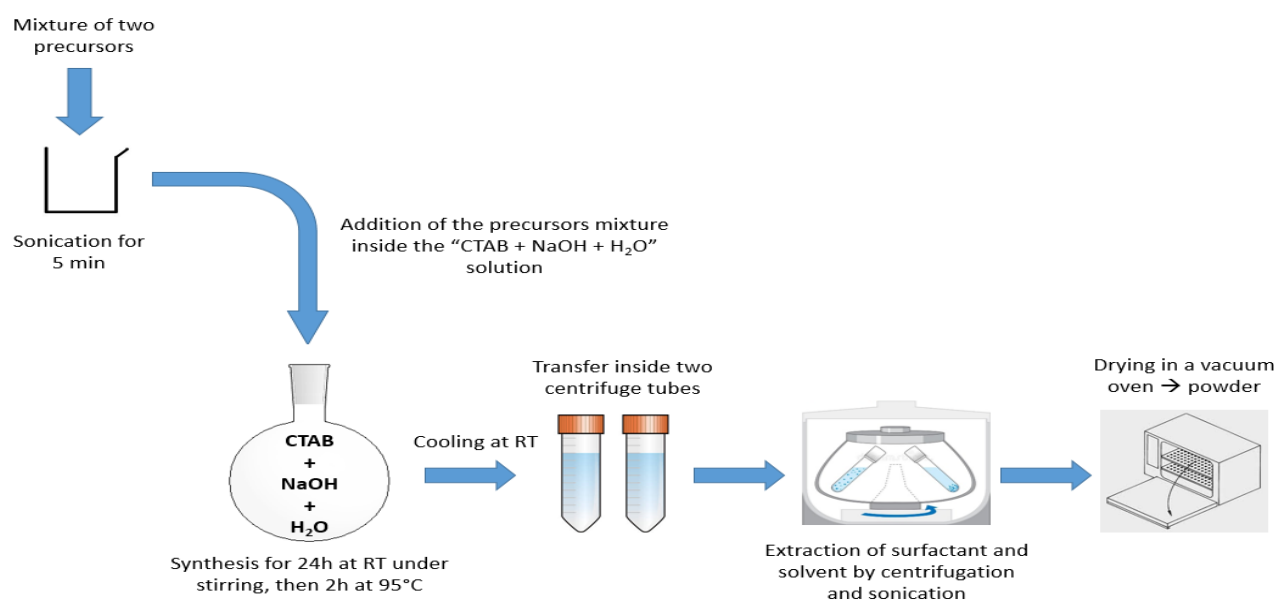


**Figure 19.** PMO NPs synthesis process with CTAB.

### 3.3. DLS Analysis

Dynamic light scattering (DLS) is a non-destructive analysis technique for measuring the hydrodynamic diameter of particles suspended in a liquid. Analysis of the scattering of light from the laser of the device by particles was performed with the Cordouan Technologies DL 135.

### 3.4. FTIR Analysis

Fourier transform infrared spectroscopy (FTIR) is a non-destructive analysis technique based on the absorption of electromagnetic radiation between 2.5 and 25  $\mu\text{m}$  (wavelength between 400 and 4000  $\text{cm}^{-1}$ ). Absorptions in this zone correspond to the movement (vibrations, rotations, etc.) of organic functional groups and can be used to deduce the chemical bonds and the structural details of the material. Analyses were performed using the Spectrum Two FT-IR Spectrometer (Perkin Elmer, Waltham, MA, USA).

### 3.5. TEM Analysis

Transmission electron microscopy (TEM) is an analytical technique which enables observation of the local pore arrangement of a material by means of the interactions that occur when an electron beam accelerated by a high voltage travels through the material. For TEM characterization, the nanoparticles of the material were dispersed in EtOH and carefully deposited on a copper grid with porous carbon films. The JEOL 1400 Plus (120 kV) microscope was used to record the image size, the shapes and the pores of the synthesized nanoparticles.

### 3.6. Textural Analysis

Prior to the sorption measurements, the nanoparticles were evacuated under a secondary vacuum at 80 °C for 8 h. Because our materials are hybrid materials, the organic moieties in the materials cannot withstand high activation temperatures. We optimized the activation temperature, and 80 °C was found to be acceptable. The nitrogen sorption isotherms showed that the mesoporosity is accessible to nitrogen, which supports our choice.

The sorption isotherms were obtained at 77 K using a Micromeritics TriStar device. The specific surface area of the various materials was derived using the BET (Brunauer-Emmet-Teller) method, taking 0.162  $\text{nm}^2$  as cross sectional area for nitrogen. T-plot analysis of the sorption isotherms revealed that the prepared materials were not microporous, which allowed the use of the BET model for deriving the specific surface areas. The pore

size distributions were derived using the BJH (Barrett-Joyner-Helenda) approach on the desorption branches of the sorption isotherms, starting from  $p/p^\circ = 0.95$  downwards. The pore geometry was assumed to be cylindrical.

### 3.7. RMN Analysis

Nuclear magnetic resonance (NMR) spectroscopy is an analytical technique for determining the structure of an organic molecule, exploiting the magnetic properties of certain atomic nuclei, such as hydrogen, carbon, or silicon. Solid  $^{13}\text{C}$ -NMR analysis was carried out on 50 mg of NPs using a VARIAN 300 MHz (Wild Bore) solid spectrometer (3.2 mm MAS probe) device.

### 3.8. Elemental Analysis

Elemental analysis is a qualitative and quantitative technique for revealing, by means of combustion or pyrolysis, the elemental composition of an organic compound and therefore the mass percentage of elements such as carbon, hydrogen, nitrogen, sulfur and oxygen. Elemental analysis was carried out using an Elementar Vario Micro Cube device with a sample of 15 mg.

### 3.9. $\text{CO}_2$ Adsorption Measurement

The  $\text{CO}_2$  adsorption isotherms were measured using a Micromeritics 3Flex device. Two sorption temperatures were investigated, namely 273 K and 298 K, in order to provide the isosteric heat of adsorption. Prior to the sorption measurements, the materials underwent a degassing stage at 80 °C for 8 h under a secondary vacuum.

## 4. Conclusions

Various syntheses of PMO NPs were successfully achieved for the  $\text{CO}_2$  capture application. A significant impact on the polycondensation between the BTEE and the aminopyridine or bipyridine (iPrbipyridine, Etbipyridine) precursors was observed, compared to the synthesis of PMO 1 NPs with 100% BTEE. Specifically, an increase in the  $\text{CO}_2$  adsorption of 29% (94% BTEE/6% iPrbipyridine;  $1.04 \text{ mmol}\cdot\text{g}^{-1}$ ), 17% (85% BTEE/15% Etbipyridine;  $0.95 \text{ mmol}\cdot\text{g}^{-1}$ ), and 14% (85% BTEE/15% aminopyridine;  $0.92 \text{ mmol}\cdot\text{g}^{-1}$ ) was observed compared to PMO 1 NPs ( $0.81 \text{ mmol}\cdot\text{g}^{-1}$ ). The addition of aminopyridine or bipyridine groups improved the affinity of the PMO with  $\text{CO}_2$ . In conclusion, PMO NPs represent an interesting tool for  $\text{CO}_2$  capture applications. Furthermore, the prepared PMO NPs could be useful for carbonate synthesis from epoxides [49] or hydrogenation of  $\text{CO}_2$  to formic acid or methanol [50].

**Supplementary Materials:** The following supporting information can be downloaded at: <https://www.mdpi.com/article/10.3390/molecules27134245/s1>, Figure S1. FTIR-ATR of pyPMO NPs. Table S1. Microanalyses of PMO1NPs and pyPMO NPs, Figure S2. DLS of PMO 1 NPs in EtOH intensity mode, Figure S3. DLS of pyPMO 6 NPs in EtOH intensity mode. Figure S4. DLS of pyPMO 15 NPs in EtOH intensity mode. Figure S5. FTIR-ATR of iPrbipyPMO NPs. Table S2, Microanalyses of PMO1 NPs and iPrbipyPMO NPs. Figure S6. DLS of iPrbipyPMO 6 NPs in EtOH intensity mode. Figure S7. DLS of iPrbipyPMO 10 NPs in EtOH intensity mode. Figure S8. DLS of iPrbipyPMO 15 NPs in EtOH intensity mode. Figure S9. FTIR-ATR of EtbipyPMO NPs. Table S3. Microanalyses of PMO1 NPs and EtbipyPMO NPs. Figure S10. DLS of EtPrbipyPMO 6 NPs in EtOH intensity mode. Figure S11. DLS of EtbipyPMO 10 NPs in EtOH intensity mode. Figure S12. DLS of EtbipyPMO 15 NPs in EtOH intensity mode.

**Author Contributions:** J.-O.D., C.C. and S.R. conceived and designed the experiments; P.K., N.B., N.D., S.R., L.R. and A.B. performed the experiments; P.K., L.B., C.C., P.T. and J.-O.D. analyzed the data; A.B., C.C., P.K., L.B. and J.-O.D. wrote the paper. All authors have read and agreed to the published version of the manuscript.

**Funding:** This research received no external funding.

**Data Availability Statement:** Not applicable.

**Acknowledgments:** ICGM staff is gratefully acknowledged for the welcome and help during the experiments. Capgemini Engineering is gratefully acknowledged for confidence throughout the project. ANR MSN 2hv is gratefully acknowledged for the N.B. grant.

**Conflicts of Interest:** The authors declare no conflict of interest.

**Sample Availability:** Not applicable.

## References

1. Jacobson, M.Z. The health and climate impacts of carbon capture and direct air capture. *Energy Environ. Sci.* **2019**, *12*, 3567–3574. [[CrossRef](#)]
2. Rae, J.W.B.; Zhang, Y.G.; Liu, X.; Foster, G.L.; Stoll, H.M.; Whiteford, R.D.M. Atmospheric CO<sub>2</sub> over the Past 66 Million Years from Marine Archives. *Annu. Rev. Earth Planet. Sci.* **2021**, *49*, 609–641. [[CrossRef](#)]
3. Han, Q.; Bai, X.; Man, Z.; He, H.; Li, L.; Hu, J.; Alsaedi, A.; Hayat, T.; Yu, Z.; Zhang, W.; et al. Convincing Synthesis of Atomically Thin, Single-Crystalline InVO<sub>4</sub> Sheets toward Promoting Highly Selective and Efficient Solar Conversion of CO<sub>2</sub> into CO. *J. Am. Chem. Soc.* **2019**, *141*, 4209–4213. [[CrossRef](#)] [[PubMed](#)]
4. Shirley, H.; Su, X.; Sanjanwala, H.; Talukdar, K.; Jurss, J.W.; Delcamp, J.H. Durable Solar-Powered Systems with Ni-Catalysts for Conversion of CO<sub>2</sub> or CO to CH<sub>4</sub>. *J. Am. Chem. Soc.* **2019**, *141*, 6617–6622. [[CrossRef](#)]
5. Kar, S.; Goepfert, A.; Prakash, G.K.S. Integrated CO<sub>2</sub> Capture and Conversion to Formate and Methanol: Connecting Two Threads. *Acc. Chem. Res.* **2019**, *52*, 2892–2903. [[CrossRef](#)]
6. Mou, S.; Wu, T.; Xie, J.; Zhang, Y.; Ji, L.; Huang, H.; Wang, T.; Luo, Y.; Xiong, X.; Tang, B.; et al. Boron Phosphide Nanoparticles: A Nonmetal Catalyst for High-Selectivity Electrochemical Reduction of CO<sub>2</sub> to CH<sub>3</sub>OH. *Adv. Mater.* **2019**, *31*, 1903499. [[CrossRef](#)]
7. Falcone, M.; Scopelliti, R.; Mazzanti, M. CO<sub>2</sub> and CO/H<sub>2</sub> Conversion to Methoxide by a Uranium(IV) Hydride. *J. Am. Chem. Soc.* **2019**, *141*, 9570–9577. [[CrossRef](#)]
8. Kamphuis, A.J.; Picchioni, F.; Pescarmona, P.P. CO<sub>2</sub>-fixation into cyclic and polymeric carbonates: Principles and applications. *Green Chem.* **2019**, *21*, 406–448. [[CrossRef](#)]
9. Chiang, C.-L.; Lin, K.-S.; Chuang, H.-W. Direct synthesis of formic acid via CO<sub>2</sub> hydrogenation over Cu/ZnO/Al<sub>2</sub>O<sub>3</sub> catalyst. *J. Clean. Prod.* **2018**, *172*, 1957–1977. [[CrossRef](#)]
10. Xu, M.; Jupp, A.R.; Ong, M.S.E.; Burton, K.I.; Chitnis, S.S.; Stephan, D.W. Synthesis of Urea Derivatives from CO<sub>2</sub> and Silylamines. *Angew. Chem. Int. Ed.* **2019**, *58*, 5707–5711. [[CrossRef](#)]
11. Boot-Handford, M.E.; Abanades, J.C.; Anthony, E.J.; Blunt, M.J.; Brandani, S.; Mac Dowell, N.; Fernández, J.R.; Ferrari, M.-C.; Gross, R.; Hallett, J.P.; et al. Carbon capture and storage update. *Energy Environ. Sci.* **2014**, *7*, 130–189. [[CrossRef](#)]
12. Haszeldine, R.S. Carbon Capture and Storage: How Green Can Black Be? *Science* **2009**, *325*, 1647–1652. [[CrossRef](#)]
13. Cavenati, S.; Grande, C.A.; Rodrigues, A.E. Adsorption Equilibrium of Methane, Carbon Dioxide, and Nitrogen on Zeolite 13X at High Pressures. *J. Chem. Eng. Data* **2004**, *49*, 1095–1101. [[CrossRef](#)]
14. Nandi, M.; Okada, K.; Dutta, A.; Bhaumik, A.; Maruyama, J.; Derks, D.; Uyama, H. Unprecedented CO<sub>2</sub> uptake over highly porous N-doped activated carbon monoliths prepared by physical activation. *Chem. Commun.* **2012**, *48*, 10283–10285. [[CrossRef](#)] [[PubMed](#)]
15. Sim, K.; Lee, N.; Kim, J.; Cho, E.-B.; Gunathilake, C.; Jaroniec, M. CO<sub>2</sub> Adsorption on Amine-Functionalized Periodic Mesoporous Benzenesilicas. *ACS Appl. Mater. Interfaces* **2015**, *7*, 6792–6802. [[CrossRef](#)] [[PubMed](#)]
16. Shi, X.; Xiao, H.; Azarabadi, H.; Song, J.; Wu, X.; Chen, X.; Lackner, K.S. Sorbents for the Direct Capture of CO<sub>2</sub> from Ambient Air. *Angew. Chem. Int. Ed.* **2020**, *59*, 6984–7006. [[CrossRef](#)]
17. Liu, J.; Thallapally, P.K.; McGrail, B.P.; Brown, D.R.; Liu, J. Progress in adsorption-based CO<sub>2</sub> capture by metal–organic frameworks. *Chem. Soc. Rev.* **2012**, *41*, 2308–2322. [[CrossRef](#)]
18. He, H.; Sun, Q.; Gao, W.; Perman, J.A.; Sun, F.; Zhu, G.; Aguila, B.; Forrest, K.; Space, B.; Ma, S. A Stable Metal–Organic Framework Featuring a Local Buffer Environment for Carbon Dioxide Fixation. *Angew. Chem. Int. Ed.* **2018**, *57*, 4657–4662. [[CrossRef](#)]
19. Zhu, J.; Usov, P.M.; Xu, W.; Celis-Salazar, P.J.; Lin, S.; Kessinger, M.C.; Landaverde-Alvarado, C.; Cai, M.; May, A.M.; Sleboznick, C.; et al. A New Class of Metal-Cyclam-Based Zirconium Metal–Organic Frameworks for CO<sub>2</sub> Adsorption and Chemical Fixation. *J. Am. Chem. Soc.* **2018**, *140*, 993–1003. [[CrossRef](#)]
20. Rachuri, Y.; Kurisingal, J.F.; Chitumalla, R.K.; Vuppala, S.; Gu, Y.; Jang, J.; Choe, Y.; Suresh, E.; Park, D.-W. Adenine-Based Zn(II)/Cd(II) Metal–Organic Frameworks as Efficient Heterogeneous Catalysts for Facile CO<sub>2</sub> Fixation into Cyclic Carbonates: A DFT-Supported Study of the Reaction Mechanism. *Inorg. Chem.* **2019**, *58*, 11389–11403. [[CrossRef](#)]
21. Li, X.-Y.; Ma, L.-N.; Liu, Y.; Hou, L.; Wang, Y.-Y.; Zhu, Z. Honeycomb Metal–Organic Framework with Lewis Acidic and Basic Bifunctional Sites: Selective Adsorption and CO<sub>2</sub> Catalytic Fixation. *ACS Appl. Mater. Interfaces* **2018**, *10*, 10965–10973. [[CrossRef](#)] [[PubMed](#)]
22. Xu, X.; Song, C.; Andresen, J.M.; Miller, B.G.; Scaroni, A.W. Novel Polyethylenimine-Modified Mesoporous Molecular Sieve of MCM-41 Type as High-Capacity Adsorbent for CO<sub>2</sub> Capture. *Energy Fuels* **2002**, *16*, 1463–1469. [[CrossRef](#)]
23. Wei, Y.; Li, X.; Zhang, R.; Liu, Y.; Wang, W.; Ling, Y.; El-Toni, A.M.; Zhao, D. Periodic Mesoporous Organosilica Nanocubes with Ultrahigh Surface Areas for Efficient CO<sub>2</sub> Adsorption. *Sci. Rep.* **2016**, *6*, 20769. [[CrossRef](#)] [[PubMed](#)]

24. De Canck, E.; Ascoop, I.; Sayari, A.; Van Der Voort, P. Periodic mesoporous organosilicas functionalized with a wide variety of amines for CO<sub>2</sub> adsorption. *Phys. Chem. Chem. Phys.* **2013**, *15*, 9792–9799. [[CrossRef](#)] [[PubMed](#)]
25. Alauzun, J.; Mehdi, A.; Reyé, C.; Corriu, R.J.P. CO<sub>2</sub> as a Supramolecular Assembly Agent: A Route for Lamellar Materials with a High Content of Amine Groups. *J. Am. Chem. Soc.* **2005**, *127*, 11204–11205. [[CrossRef](#)] [[PubMed](#)]
26. Nigar, H.; Garcia-Baños, B.; Peñaranda-Foix, F.L.; Catalá-Civera, J.M.; Mallada, R.; Santamaría, J. Amine-functionalized mesoporous silica: A material capable of CO<sub>2</sub> adsorption and fast regeneration by microwave heating. *AIChE J.* **2016**, *62*, 547–555. [[CrossRef](#)]
27. Knowles, G.P.; Delaney, S.W.; Chaffee, A.L. Diethylenetriamine[propyl(silyl)]-Functionalized (DT) Mesoporous Silicas as CO<sub>2</sub> Adsorbents. *Ind. Eng. Chem. Res.* **2006**, *45*, 2626–2633. [[CrossRef](#)]
28. Vilarrasa-García, E.; Cecilia, J.A.; Moya, E.M.O.; Cavalcante, C.L.; Azevedo, D.C.S.; Rodríguez-Castellón, E. “Low Cost” Pore Expanded SBA-15 Functionalized with Amine Groups Applied to CO<sub>2</sub> Adsorption. *Materials* **2015**, *8*, 2495–2513. [[CrossRef](#)]
29. Yu, L.; Kanezashi, M.; Nagasawa, H.; Tsuru, T. Role of Amine Type in CO<sub>2</sub> Separation Performance within Amine Functionalized Silica/Organosilica Membranes: A Review. *Appl. Sci.* **2018**, *8*, 1032. [[CrossRef](#)]
30. Croissant, J.G.; Cattoen, X.; Wong Chi Man, M.; Durand, J.-O.; Khashab, N.M. Syntheses and applications of periodic mesoporous organosilica nanoparticles. *Nanoscale* **2015**, *7*, 20318–20334. [[CrossRef](#)]
31. Liu, X.; Maegawa, Y.; Goto, Y.; Hara, K.; Inagaki, S. Heterogeneous Catalysis for Water Oxidation by an Iridium Complex Immobilized on Bipyridine-Periodic Mesoporous Organosilica. *Angew. Chem. Int. Ed.* **2016**, *55*, 7943–7947. [[CrossRef](#)] [[PubMed](#)]
32. Kuramochi, Y.; Sekine, M.; Kitamura, K.; Maegawa, Y.; Goto, Y.; Shirai, S.; Inagaki, S.; Ishida, H. Photocatalytic CO<sub>2</sub> Reduction by Periodic Mesoporous Organosilica (PMO) Containing Two Different Ruthenium Complexes as Photosensitizing and Catalytic Sites. *Chem. A Eur. J.* **2017**, *23*, 10301–10309. [[CrossRef](#)] [[PubMed](#)]
33. Wang, X.; Thiel, I.; Fedorov, A.; Copéret, C.; Mougél, V.; Fontecave, M. Site-isolated manganese carbonyl on bipyridine-functionalities of periodic mesoporous organosilicas: Efficient CO<sub>2</sub> photoreduction and detection of key reaction intermediates. *Chem. Sci.* **2017**, *8*, 8204–8213. [[CrossRef](#)] [[PubMed](#)]
34. Waki, M.; Yamanaka, K.-i.; Shirai, S.; Maegawa, Y.; Goto, Y.; Yamada, Y.; Inagaki, S. Re(bpy)(CO)<sub>3</sub>Cl Immobilized on Bipyridine-Periodic Mesoporous Organosilica for Photocatalytic CO<sub>2</sub> Reduction. *Chem. A Eur. J.* **2018**, *24*, 3846–3853. [[CrossRef](#)]
35. Cho, H.S.; Lee, Y.; Wu, J.; Shin, S.R.; Kang, J.K.; Terasaki, O. Understanding Adsorption Behavior of Periodic Mesoporous Organosilica Having a Heterogeneous Chemical Environment: Selective Coverage and Interpenetration of Adsorbates inside the Channel Wall. *J. Phys. Chem. C* **2019**, *123*, 24884–24889. [[CrossRef](#)]
36. Waki, M.; Shirai, S.; Yamanaka, K.-I.; Maegawa, Y.; Inagaki, S. Heterogeneous water oxidation photocatalysis based on periodic mesoporous organosilica immobilizing a tris(2,2′-bipyridine)ruthenium sensitizer. *RSC Adv.* **2020**, *10*, 13960–13967. [[CrossRef](#)]
37. Yamaguchi, S.; Hashimoto, S. Mechanism of Formic Acid Disproportionation Catalyzed by an Iridium Complex Immobilized on Bipyridine-Periodic Mesoporous Organosilica: A Case Study Based on Kinetics Analysis. *Asian J. Org. Chem.* **2020**, *9*, 99–104. [[CrossRef](#)]
38. Cho, E.J.; Kang, J.K.; Jung, J.H. A mesoporous silica functionalized by a covalently bound pyridine derivative for selective optical sensing of thymidine. *Mater. Lett.* **2007**, *61*, 5157–5160. [[CrossRef](#)]
39. Zhou, X.; Yi, H.; Tang, X.; Deng, H.; Liu, H. Thermodynamics for the adsorption of SO<sub>2</sub>, NO and CO<sub>2</sub> from flue gas on activated carbon fiber. *Chem. Engin. J.* **2012**, *200–202*, 399–404. [[CrossRef](#)]
40. Gelles, T.; Lawson, S.; Rownaghi, A.A.; Rezaei, F. Recent advances in development of amine functionalized adsorbents for CO<sub>2</sub> capture. *Adsorption* **2020**, *26*, 5–50. [[CrossRef](#)]
41. Chen, C.; Kim, J.; Ahn, W.-S. CO<sub>2</sub> capture by amine-functionalized nanoporous materials: A review. *Korean J. Chem. Eng.* **2014**, *31*, 1919–1934. [[CrossRef](#)]
42. Mello, M.R.; Phanon, D.; Silveira, G.Q.; Llewellyn, P.L.; Ronconi, C.M. Amine-modified MCM-41 mesoporous silica for carbon dioxide capture. *Microporous Mesoporous Mater.* **2011**, *143*, 174–179. [[CrossRef](#)]
43. Kim, S.; Ida, J.; Gulians, V.V.; Lin, Y.S. Tailoring Pore Properties of MCM-48 Silica for Selective Adsorption of CO<sub>2</sub>. *J. Phys. Chem. B* **2005**, *109*, 6287–6293. [[CrossRef](#)] [[PubMed](#)]
44. Franchi, R.S.; Harlick, P.J.E.; Sayari, A. Applications of Pore-Expanded Mesoporous Silica. 2. Development of a High-Capacity, Water-Tolerant Adsorbent for CO<sub>2</sub>. *Ind. Eng. Chem. Res.* **2005**, *44*, 8007–8013. [[CrossRef](#)]
45. Schumacher, C.; Gonzalez, J.; Pérez-Mendoza, M.; Wright, P.A.; Seaton, N.A. Design of Hybrid Organic/Inorganic Adsorbents Based on Periodic Mesoporous Silica. *Ind. Eng. Chem. Res.* **2006**, *45*, 5586–5597. [[CrossRef](#)]
46. Xu, X.; Song, C.; Andrésen, J.M.; Miller, B.G.; Scaroni, A.W. Preparation and characterization of novel CO<sub>2</sub> “molecular basket” adsorbents based on polymer-modified mesoporous molecular sieve MCM-41. *Microporous Mesoporous Mater.* **2003**, *62*, 29–45. [[CrossRef](#)]
47. Stephenson, R.M.; Malanowski, S.; Ambrose, D. *Handbook of the Thermodynamics of Organic Compounds*; Elsevier: New York, NY, USA, 1987.
48. Sun, L.; Mai, W.; Dang, S.; Qiu, Y.; Deng, W.; Shi, L.; Yan, W.; Zhang, H. Near-infrared luminescence of periodic mesoporous organosilicas grafted with lanthanide complexes based on visible-light sensitization. *J. Mater. Chem.* **2012**, *22*, 5121–5127. [[CrossRef](#)]

49. Azzouz, R.; Moreno, V.C.; Herasme-Grullon, C.; Levacher, V.; Estel, L.; Ledoux, A.; Derrouiche, S.; Marsais, F.; Bischoff, L. Efficient Conversion of Epoxides into Carbonates with CO<sub>2</sub> and a Single Organocatalyst: Laboratory and Kilogram-Scale Experiments. *Synlett* **2020**, *31*, 183–188. [[CrossRef](#)]
50. Umegaki, T.; Enomoto, Y.; Kojima, Y. Metallic ruthenium nanoparticles for hydrogenation of supercritical carbon dioxide. *Catal. Sci. Technol.* **2016**, *6*, 409–412. [[CrossRef](#)]